Conference paper

Lucie Speyer, Océane Louppe, Sébastien Fontana, Sébastien Cahen* and Claire Hérold

Toward the control of graphenic foams

DOI 10.1515/pac-2016-1117

Abstract: Graphene-based materials are extensively studied, due to their excellent properties and their wide range of possible applications. Attention has recently been paid to three-dimensional-like graphenic structures, such as crumpled graphene sheets and graphenic foams: these kinds of materials can combine the properties of graphene associating high surface area and porosity, what is particularly interesting for energy or catalysis applications. Most of the synthesis methods leading to such structures are based on graphite oxide exfoliation and re-assembly, but in this work we focus on the preparation of graphenic foams by a solvothermal-based process. We performed a solvothermal reaction between ethanol and sodium at 220 °C, during 72 h, under 200 bar, followed by a pyrolysis under nitrogen flow. An extended study of the influence of the temperature (800 °C–900 °C) of pyrolysis evidences an unexpected strong effect of this parameter on the characteristics of the materials. The optimal conditions provide multi-layer graphene (10 layers) foam with a surface area of 2000 $m^2 \cdot g^{-1}$. This work is an important step for the understanding of the mechanisms of the thermal treatment. Post-treatments in different experimental conditions are performed in order to modulate the structure and properties of the graphenic foams.

Keywords: adsorption; carbon compounds; solid-state chemistry; X-ray diffraction; Raman spectroscopy; SSC-2016.

Introduction

Riding the wave of the intensive research on graphene elaboration, properties, and potentialities [1], a great interest has more recently been paid to three-dimensional graphene-like structures: graphene sheets interconnected to form macroscopic three-dimensional (3D) materials [2–4]. The presence of defects, curvatures and dangling bonds prevents the aggregation of the graphene layers, which develop porous structures with high accessible surface areas [5]. Combined with the properties of graphene, especially transport properties, these materials are promising for application domains such as energy (electrode materials for various energy storage or conversion devices [6–12]).

While very diversified methods have been developed these last years for the preparation of graphene-related materials (mechanical exfoliation [13], liquid-phase exfoliation [14–16], chemical vapor deposition on metal surfaces [17], growth on SiC surfaces [18], molecular assembly [19]), the use of graphite oxide is the most widespread for 3D graphenic materials. Indeed, it can be obtained in large quantities by chemical treatments of graphite in acid and oxidizing media [20]. Thermal reduction of solid graphite oxide [21] or graphite oxide aqueous dispersions [22] have been reported, as well as liquid-phase assembly or template methods [23, 24].

Article note: A collection of invited papers based on presentations at the 12th Conference on Solid State Chemistry (SSC-2016), Prague, Czech Republic, 18–23 September 2016.

***Corresponding author: Sébastien Cahen,** Institut Jean Lamour, UMR 7198 CNRS – Université de Lorraine, Faculté des Sciences et Technologies, B.P. 70239, 54506 Vandœuvre-lès-Nancy cedex, France, e-mail: sebastien.cahen@univ-lorraine.fr
Lucie Speyer: Institut Français du Pétrole et des Energies Nouvelles, Rond-point de l'échangeur de Solaize, BP 3, 69360 Solaize, France
Océane Louppe, Sébastien Fontana and Claire Hérold: Institut Jean Lamour, UMR 7198 CNRS – Université de Lorraine, Faculté des Sciences et Technologies, B.P. 70239, 54506 Vandœuvre-lès-Nancy cedex, France

Our work is focused on a bottom-up solvothermal-based elaboration of 3D graphenic structures, developed in 2009 by Choucair et al. [25] and taken up by a few other studies. It is a process consisting in a solvothermal reaction between metallic sodium and an alcohol, followed by a rapid thermal treatment in air of the as-obtained sodium ethoxide, and finally a washing in an acid medium. The samples have great potentialities as electrode materials for supercapacitors [26], lithium-ion batteries [27, 28] or fuel cells [29, 30]. Here we perform for the thermal treatment a long pyrolysis under a nitrogen flow which provides high-quality graphenic foams (compared to those obtained after a thermal treatment in air) with elevated specific surface areas [31]. Our previous work concerning the conditions of temperature and time of pyrolysis indicates a very strong influence of these parameters on the different features of the samples. We particularly evidenced a necessary compromise between the structural quality of the graphenic foams and the stabilization of mineral impurities, mostly sodium carbonate, providing from the thermal decomposition of sodium ethoxide. In this work, we present a better optimization of the thermal treatment conditions, and then we carried out post-elaboration treatments on carbon-based materials to increase the purity and the structural properties of the samples.

Indeed, it is well known that annealing treatments under vacuum or inert atmosphere improve the quality of carbon materials. The thermal energy intake lead to the rearrangement of amorphous carbon [32, 33], especially on graphene surfaces [34], which could be very attractive to eliminate eventual disordered phases contained in the graphenic foams. The in-plane crystalline quality is widely improved too [32, 33]. Annealing treatments also improve the graphitization along the $\vec{c}$ axis, notably through a structuration of turbostratic stacking to hexagonal stacking [35]. Furthermore, vacuum annealing could be a solution to eliminate trapped sodium carbonate contained in the solvothermal graphenic foams. This treatment has been shown to be very efficient to remove, for example, mineral impurities from carbon nanotubes samples [36, 37]. Then, vacuum annealing appears to be particularly adapted to improve the characteristics of the graphenic foams obtained by solvothermal reaction and pyrolysis, as their structural quality as their chemical purity.

Experimental

Elaboration

The elaboration of the graphenic foams is completed as described elsewhere [31] by a solvothermal reaction between sodium and ethanol. Under inter atmosphere (argon, Air Liquide Alphagaz 1), 15 mL of anhydrous ethanol and 6 g of metallic sodium are mixed together in a Parr autoclave of 0.5 L volume. Then, a pressure of 100 bar is introduced in the reactor by injection of nitrogen (Air Liquide, Alphagaz 2). The reactor is then heated at 220 °C for 72 h (the internal pressure reaches 200 bar) and finally cooled down naturally to room temperature. The sodium ethoxide solvothermal product in then collected and pyrolysed under a nitrogen flow between 800 °C and 900 °C for 4 h. The reaction yields carbon, sodium carbonate, sodium hydroxide and gaseous hydrocarbons. The obtained powder is then sonicated in ethanol and washed with 1 L of 6 mol · L^{-1} HCl and 1 L of water in order to remove sodium compounds. The final sample is finally dried at 100 °C for 24 h.

Post-elaboration treatments

In order to improve the structural quality of graphenic foams and remove mineral impurities, the obtained sample after pyrolysis at 850 °C for 4 h is annealed under secondary vacuum. A portion of 50 mg of graphene foam is introduced in a vitreous carbon crucible, inside a horizontal oven. The furnace is then evacuated ($<10^{-6}$ mbar) and heated to fixed conditions of temperature (1000 °C, 1250 °C or 1500 °C) for 1 h and cooled down naturally to room temperature under vacuum.

Characterization

Transmission electron microscopy (TEM) investigations were performed with a Jeol ARM 200F – cold FEG TEM/STEM microscope running at 80 keV. Samples were previously dispersed in ethanol and deposited on a copper grid with a holey carbon film. For thermogravimetric analysis (TGA), around 3 mg of sample were placed in a platinum crucible and analyzed under dry air on a range 20 °C–1000 °C with a heating rate of 3 °C · min^{-1} with a Setsys 1750 Evolutions Setaram device. For Raman spectroscopy, samples were dispersed in absolute ethanol and deposited on a glass lamella, then analyzed with a Horiba Jobin-YvonLabRAM HR800 spectrometer operating at the red radiation ($\lambda = 633$ nm) on the spectral ranges 900–1800 cm^{-1} (D, G and D′ bands) and 2500–2850 cm^{-1} (2D band). Adsorption isotherms (N_2, 77.3 K) were collected with a Micromeritics ASAP 2020 adsorption apparatus. Before analysis, samples were outgassed during 12 h at 400 °C. Specific surface areas were calculated using the BET model [38] (completed with the Rouquerol correction [39]). The BET method is not suitable for microporous materials such as graphene foams, despite its current use [40]. Then a calculation of the specific surface area was performed using the 2D-NLDFT [41] model, as well as the determination of the micropore volumes and pore size distributions. 2D-NLDFT calculations are carried out using SAIEUS software, with a corrugation parameter $\lambda = 4.375$ and an integration range from 0.36 to 50 nm.

Results and discussion

Five temperatures of pyrolysis were studied: 800 °C, 825 °C, 850 °C, 875 °C and 900 °C. This range of temperature has been selected after a preliminary work [31] showing that lower temperatures provide only amorphous carbon. Figure 1 presents the TEM bright-field micrographs of the corresponding samples. The five samples are characterized by fine carbon particles more or less ordered and structural differences are observed when the pyrolysis temperature increases.

In the case of pyrolyses performed at 800 °C and 825 °C, the crystallization appears incomplete, while from 850 °C, samples present a better crystalline quality with more ordered planar regions. For these temperatures, the micrographs show larges particles with the typical graphenic foam structure: very thin particles composed with stacked and curved graphitic layers. Some amorphous carbon can be observed for all samples. It is worth noting that TEM provides only local information about a little portion of the sample, so it is not sufficient to define a general trend concerning the influence of the temperature of the pyrolysis.

X-ray diffractograms of the five samples are presented (Fig. 2). They reveal the presence of several carbon phases: hexagonal graphite (space group $P6_3/mmc$, a = 246 pm, c = 671 pm), and a set of graphitic structures with stacking faults noted turbostratic carbons (space group $P6_3/mmc$ or $R\bar{3}m$, a = 252 pm, c varying from 412 pm to 4324 pm) and orthorhombic carbon (space group *Cmma*, a = 458 pm, b = 530 pm, c = 563 pm). From 850 °C, the patterns reveal a supplementary crystalline phase: sodium carbonate, resulting from the reaction of pyrolysis. Despite the washing step with hydrochloric acid, sodium carbonate remains present in the samples, certainly because it is trapped into cavities of the graphene structures. As temperature rises, the intensity of the (002) Bragg peak of hexagonal graphite increases, indicating a clear improvement of the crystallinity along the $\vec{c}$ axis as confirmed by calculation of the crystallite size along the $\vec{c}$ axis of the hexagonal graphite using the Debye-Scherrer equation. The results of the calculation are not performed for samples pyrolysis at 800 °C and 825 °C since the diffraction peak is broad and slightly intense, are reported Table 1. As expected, the corresponding number of stacked graphitic layers increases with the augmentation of the temperature of pyrolysis and varies from 11 to 22.

Raman spectroscopy is a very common technique for the study of carbon materials. The spectra corresponding to the five samples are presented (Fig. 3). They exhibit five components typically observed in graphene foam materials:

- the G band (around 1580 cm^{-1}) which corresponds to the in-plane vibration in graphite or graphene [44];
- the D and D′ bands (around 1335 and 1620 cm^{-1}), related to the defects and the edges of the graphene layers [44, 45];

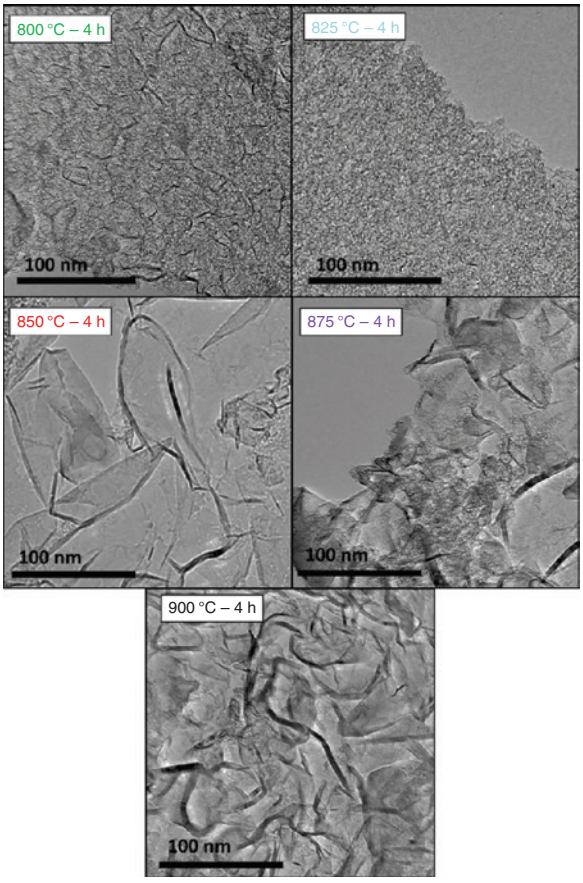

Fig. 1: TEM bright-field micrographs of the sample pyrolyzed during 4 h at 800 °C, 825 °C, 850 °C, 875 °C, 900 °C (incident beam energy 80 keV).

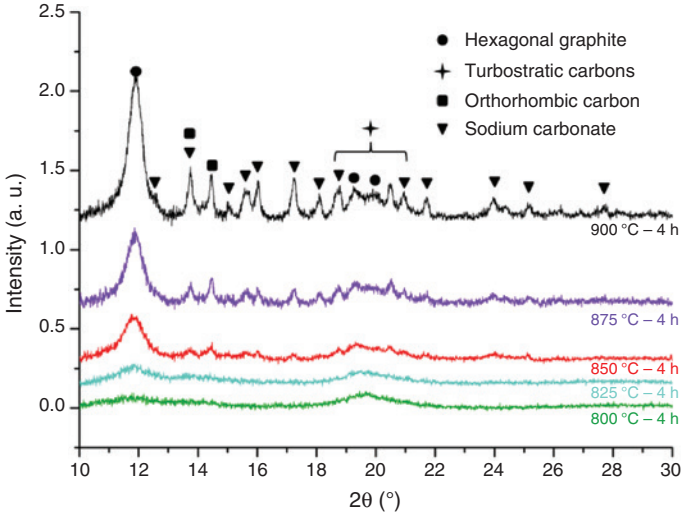

Fig. 2: Diffractograms of the samples pyrolyzed during 4 h at 800 °C, 825 °C, 850 °C, 875 °C and 900 °C fully indexed with hexagonal graphite (PDF file n° 04-007-2081), orthorhombic carbon [42], turbostratic carbons [43] and sodium carbonate (PDF file n° 04-010-2762).

Table 1: Crystallite size along the $\vec{c}$ axis and corresponding number of stacked graphitic layers calculated by the Debye-Scherrer equation.

Temperature of pyrolysis (°C)	L_c (nm)	Number of stacked graphene layers
850	3.8	11
875	5.3	16
900	7.5	22

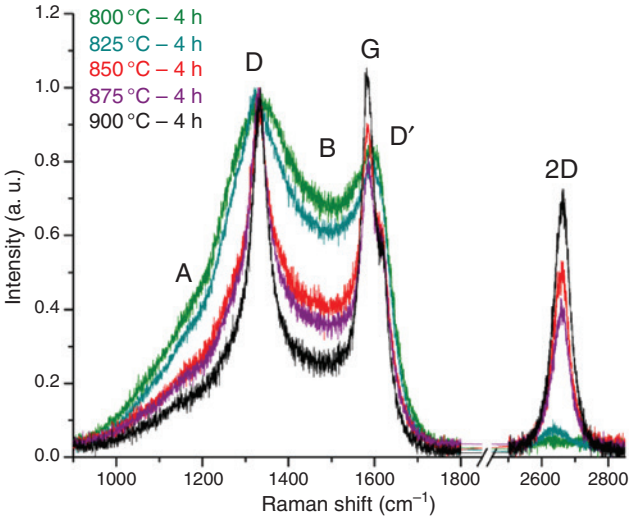

Fig. 3: Normalized Raman spectra (λ = 633 nm) for the samples pyrolyzed during 4 h at 800 °C, 825 °C, 850 °C, 875 °C and 900 °C.

- a band around 1180 cm^{-1}, called A band here, matching to sp^3 defects [46];
- a band around 1490 cm^{-1}, here called B band, corresponding to aromatic clusters in disordered carbons [47] or nanocrystalline graphite [48].

Raman spectrum of each sample shows the characteristic vibration bands. The latter are strongly broadened, in particular for the lower pyrolysis temperatures.

Curve fitting was performed on the 900–1800 cm^{-1} region using Lorentzian curves for A, D and G bands [48, 49], Gaussian curve for B band [49] and a Breit-Wigner-Fano contribution for D′ band [45]. The in-plane crystalline quality of the graphene layers is studied through the joint evolution of the intensity ratio I_D/I_G of the D and G bands, and with the full width at half maximum of the G band FWHM(G) [47] (Figure 4a and b). When the pyrolysis temperature increases, a diminution in the I_D/I_G ratio and FWHM(G) is observed with an increased emphasis to 850 °C. Thus a higher temperature promotes the in-plane crystallization. Concerning the amorphous carbon, the intensity of the A and B bands decreases when the pyrolysis temperature increases (Figure 4c and d): the disordered phases contained in the sample are removed with an augmentation of the pyrolysis temperature, in particular from 850 °C. The 2D bands are almost inexistent for the temperatures 800 °C and 825 °C, and show a marked increase in intensity above 850 °C, confirming the formation of the graphitic network. These results are in agreement with TEM observations and XRD measurements.

Thermogravimetric analysis under dry air was performed to evaluate the purity and the combustion temperature of the different carbon phases. Corresponding thermograms (Fig. 5) of the five samples exhibit a main mass loss between 400 °C and 500 °C assigned to the combustion of carbon phases. Although the XRD and Raman measurements exhibit the presence of several carbon structures, only one single mass loss is

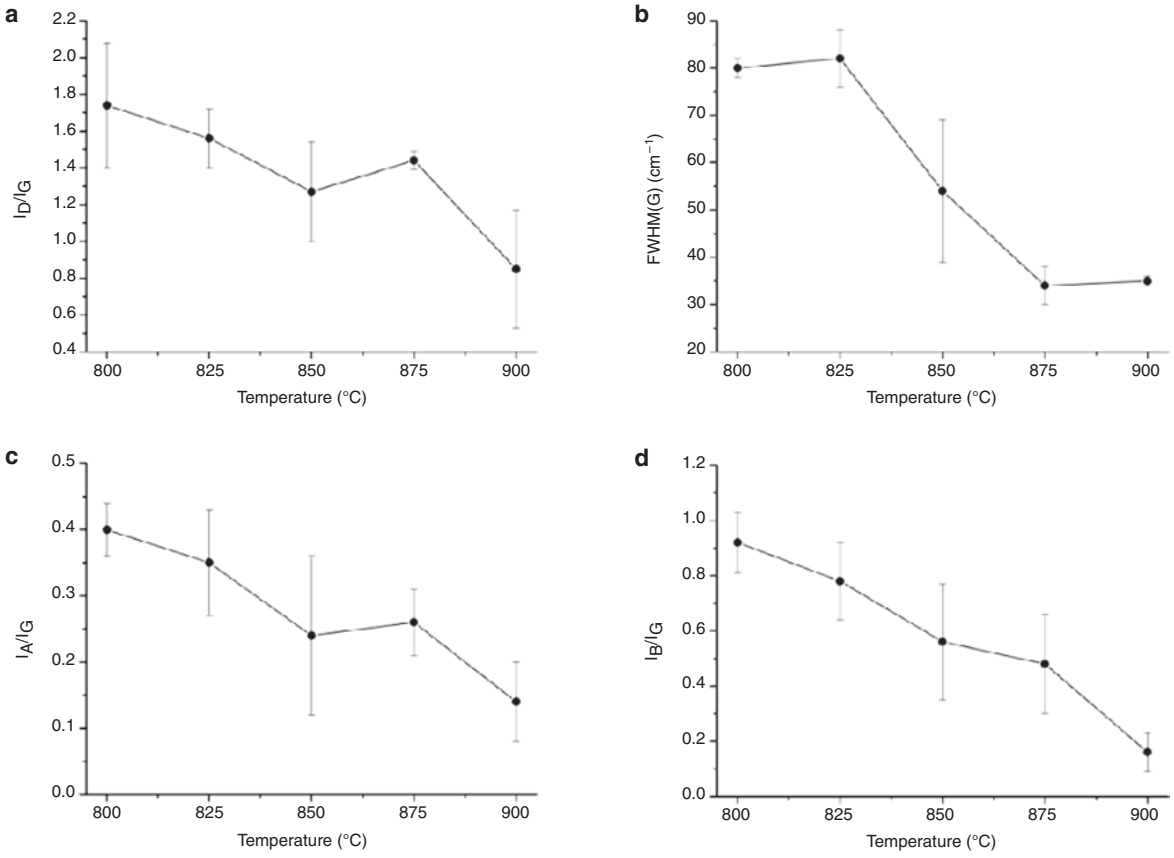

Fig. 4: (a) I_D/I_G (b) FWHM(G), (c) I_A/I_G (d) I_B/I_G parameters calculated from the deconvolution of the Raman spectra for the sample pyrolyzed during 4 h at 800 °C, 825 °C, 850 °C, 875 °C and 900 °C.

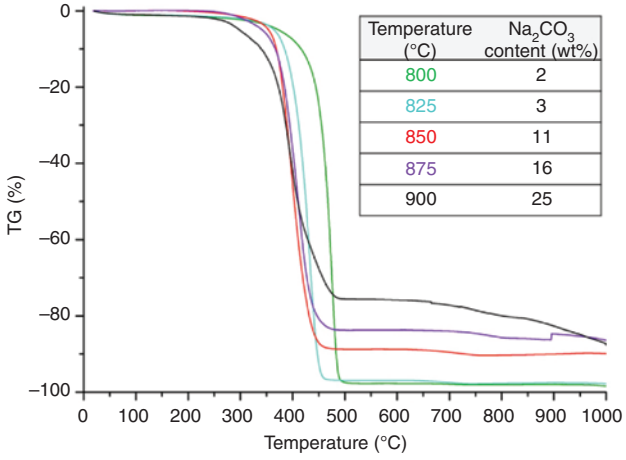

Fig. 5: TG curves (dry air, heating rate 3 °C · min^{-1}) of the sample previously pyrolyzed during 4 h at 800 °C, 825 °C, 850 °C, 875 °C and 900 °C.

observed, indicating that these structures have very similar combustion temperatures. Only the sample pyrolyzed at 900 °C leads to a two-stage combustion. For all samples, the final mass loss does not reach 100 %, contrary to what is expected for a pure carbon material whose oxidation is completed at 1000 °C. This phenomenon is attributed to the presence of residual sodium carbonate detected by XRD, progressively degraded

above 850 °C to form sodium oxide Na_2O. When the pyrolysis treatment temperature increases, the samples become less pure, due to the increased stability of the sodium carbonate whose mass content may reach 25 % at 900 °C. These observations are consistent with the XRD measurements.

Physisorption of nitrogen at 77K was conducted in order to characterize the pore structure of the samples (Fig. 6a). The adsorbed quantities and resulting values as specific surface area and pore volumes of only carbon material are deduced from the sodium carbonate content, determined by TGA. Pore size distributions are shown Fig. 6b and specific surface areas and pore volumes are presented in Table 2. The five curves are mixtures of type I, II and IV isotherms according to the IUPAC classification [40]. The important increase of the adsorbed gas at very low pressures (type I) is due to the presence of micropores, which may be attributed to the amorphous carbon and tortuosity of the samples. Type II is related to graphene surface and the hysteresis loops characterize the existence of mesopores.

The specific surface areas of the five samples are very high and indicate a large surface developed by the graphene foam structure. For the almost pyrolysis temperatures, the surface areas are higher than the values reported in the literature for graphene foams obtained by solvothermal-based process [29]. When the pyrolysis temperature increases, a diminution of the specific surface area and of the pore volume, more pronounced above 850 °C, is observed. This phenomenon is assigned to the decrease of the microporous carbon content, in agreement with Raman spectroscopy. Moreover, the augmentation of the crystallite size along the $\vec{c}$ axis as the pyrolysis temperature increases (cf. XRD measurements) tends to decrease the accessible adsorption sites for the nitrogen molecules. The size distributions are in agreement with the isotherms shape: they present well defined distribution to 0.5 nm and 0.9 nm, and a broader distribution between 1.5 and 7 nm. They are similarly shaped, regardless of the pyrolysis temperature.

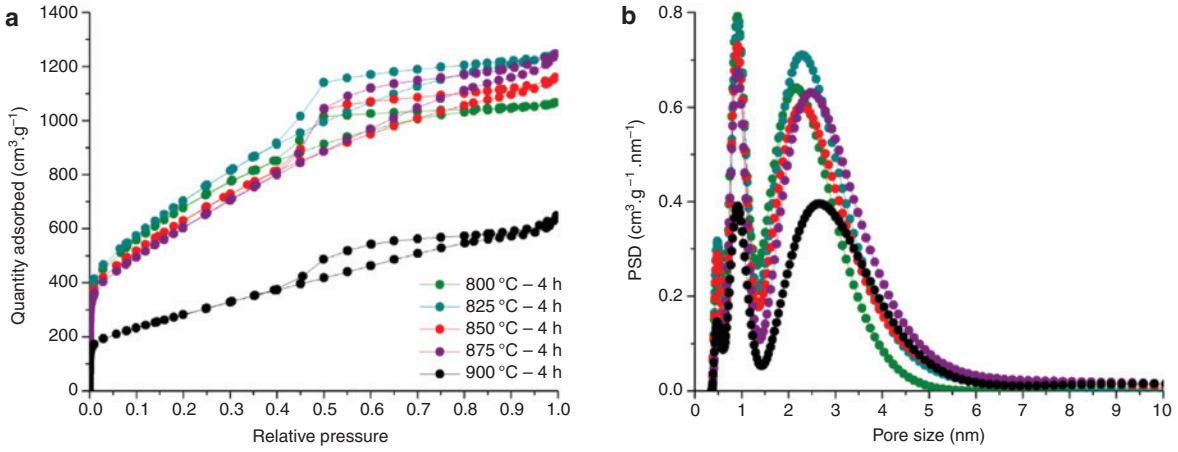

Fig. 6: (a) Adsorption isotherms (N_2 77.3 K) and (b) corresponding pore size distributions (2D-NLDFT model) of the samples pyrolyzed during 4 h at 800 °C, 825 °C, 850 °C, 875 °C and 900 °C.

Table 2: Specific surface area (BET and 2D-NLDFT models), micropore volume, total pore volume (2D-NLDFT model) of the samples pyrolyzed during 4 h at 800 °C, 825 °C, 850 °C, 875 °C and 900 °C.

Temperature of pyrolysis (°C)	BET specific area ($m^2 \cdot g^{-1}$)	2D-NLDFT specific surface area ($m^2 \cdot g^{-1}$)	2D-NLDFT micropore volume ($cm^3 \cdot g^{-1}$)	2D-NLDFT total pore volume ($cm^3 \cdot g^{-1}$)
800	2493	1908	0.71	1.52
825	2579	1997	0.66	1.79
850	2316	1809	0.59	1.67
875	2229	1722	0.49	1.79
900	1370	1108	0.28	1.23

The various techniques employed to characterize the pyrolyzed samples for 4 h at five different temperatures show a very strong influence of the pyrolysis temperature on morphology, structural quality, thickness as well as chemical purity. For temperatures below 850 °C, the samples are poorly crystallized. From 850 °C, the formation of graphenic foams begins and the temperature increase leads to an augmentation of the structural quality but a too high temperature will stabilize sodium carbonate. It has been showed through this study that the improvement of the crystalline quality of the graphenic samples is coupled with stabilization of sodium carbonate. In the light of the obtained results, we can determine the optimal conditions of synthesis. The sample pyrolyzed at 850 °C during 4 h offers the best compromise between the in-plane crystalline quality, the thickness, the amorphous carbon content, the purity and the final yield. The mechanism of formation appears quite complex. During the thermal decomposition of sodium ethoxide, it generates gaseous hydrocarbons and carbon, sodium hydroxide and sodium carbonate as solid products. Sodium compounds present in the reaction medium certainly influence the final carbon structure. In order to improve the quality of these foams, we so realized high-temperature annealing.

High-temperature annealing

In order to get an overview of the effects of vacuum annealing on the samples we annealed the sample pyrolyzed at 850 °C for 4 h (denoted raw), during 1 h at 1000 °C, 1250 °C and 1500 °C. The resulting samples are respectively named a-1000, a-1250 and a-1500. Figure 7 presents the TEM bright-field micrographs for the raw sample and samples annealed at the extremal temperatures 1000 °C and 1500 °C.

The samples maintain the typical structure of the raw graphenic foam without apparent modification, irrespective of the annealing temperature. X-ray diffraction measurements helped to calculate the crystallite size along the $\vec{c}$ axis for the three annealed samples (Table 3).

Then, in accordance with TEM observations, vacuum annealing does not lead to a too strong graphitization along the $\vec{c}$ axis. The disordered carbon phases in contact with the graphenic structure constituting the walls of the foams may rearrange and contribute to the formation of new stacked graphene layers [34]. This phenomenon can explain the little increase of the L_c parameter.

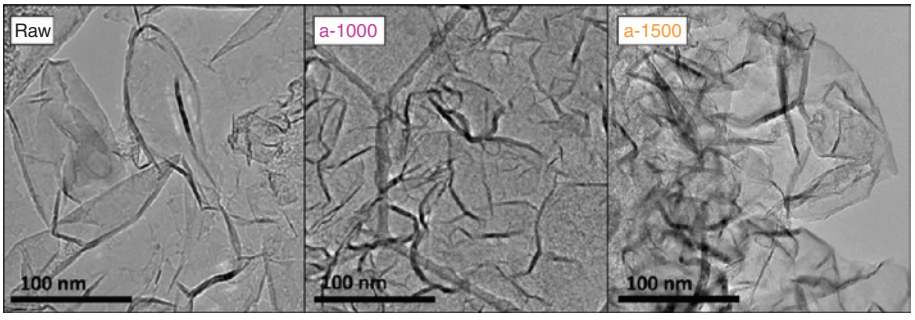

Fig. 7: TEM bright-field micrographs of the samples raw, a-1000 and a-1500.

Table 3: Crystallite size along the $\vec{c}$ axis and corresponding number of stacked graphitic layers calculated by the Debye-Scherrer equation.

Sample	L_c (nm)	Number of stacked graphene layers
Raw	3.8	11
a-1000	3.8	11
a-1250	4.1	12
a-1500	4.6	14

To confirm hypothesis, Raman analyses are realized. Raman spectra for raw and annealed samples are shown (Fig. 8). The parameters deduced from deconvolution (I_D/I_G, FWHM(G), I_A/I_G and I_B/I_G) are presented as a function of the annealing temperature (Fig. 9).

The decrease of both I_D/I_G ratio and FWHM(G) after annealing when increasing the temperature of treatment denotes the augmentation of the in-plane crystalline quality of the graphenic foam. Also, the disordered carbon content indicated by I_A/I_G and I_B/I_G ratios decreases when the temperature of annealing increases. These results, in good accordance with the literature [32–34], reveal an increase of the global structural quality of the samples after treatment, this effect being accentuated for the highest annealing temperature. The 2D bands remain almost identical after annealing and with the annealing temperature, which confirms the absence of significant modification of the stacking order evidenced by XRD.

The thermograms of the raw and annealed samples are plotted (Fig. 10). The annealed samples all exhibit the sodium carbonate content less than that of the raw sample. This indicates that almost all sodium carbonate is removed by annealing at 1000 °C. A shift of the combustion temperatures of the carbon phases towards the high temperatures is clearly observed for the annealed samples, and increases with the temperature. It confirms the augmentation of the structural quality of the samples, enhancing their thermal stability, first evidenced by Raman spectroscopy. Interestingly, the second mass loss corresponding to sodium carbonate decomposition is absent for the annealed samples. These ones are almost pure in carbon, indicating the efficient elimination of sodium carbonate what is also observed by X-ray diffraction too.

The evolution of the textural properties of the annealed foams is studied with nitrogen adsorption: isotherms and pore size distributions are presented (Fig. 11), and Table 4 lists the specific surface areas and micropore volume of the samples.

The micropore volume and specific surface area of the samples decrease with annealing, which is also observed on the pore size distributions. This is consistent with the literature which reports the degradation of the microporosity with high-temperature treatments [35, 50], by rearrangement as more ordered carbon phases or by blocking of the micropores. However, the porosity and specific surface area of the annealed samples remain consequent, in accordance with TEM observations which indicate the conservation of the graphene foam structure.

The modification of the textural and structural properties of the graphene foams after annealing is concomitant with the elimination of Na_2CO_3. In fact, during annealing Na_2CO_3 decomposes to form Na_2O and CO_2 at 851 °C, then Na_2O sublimates at 1275 °C, these two reactions occurring at lower temperatures under vacuum, the as-formed vapors may oxidize the carbon structure, and form supplementary micropores which are, in the same time, eliminated by exposition to high temperatures. A little deformation of the foam structure by

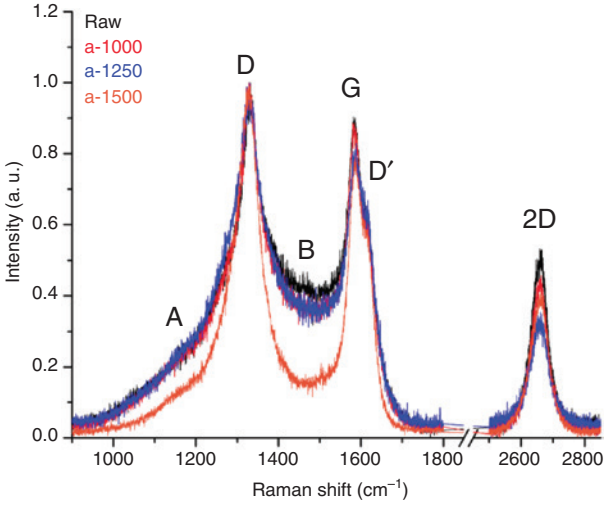

Fig. 8: Normalized Raman spectra (λ = 633 nm) for samples raw, a-1000, a-1250 and a-1500.

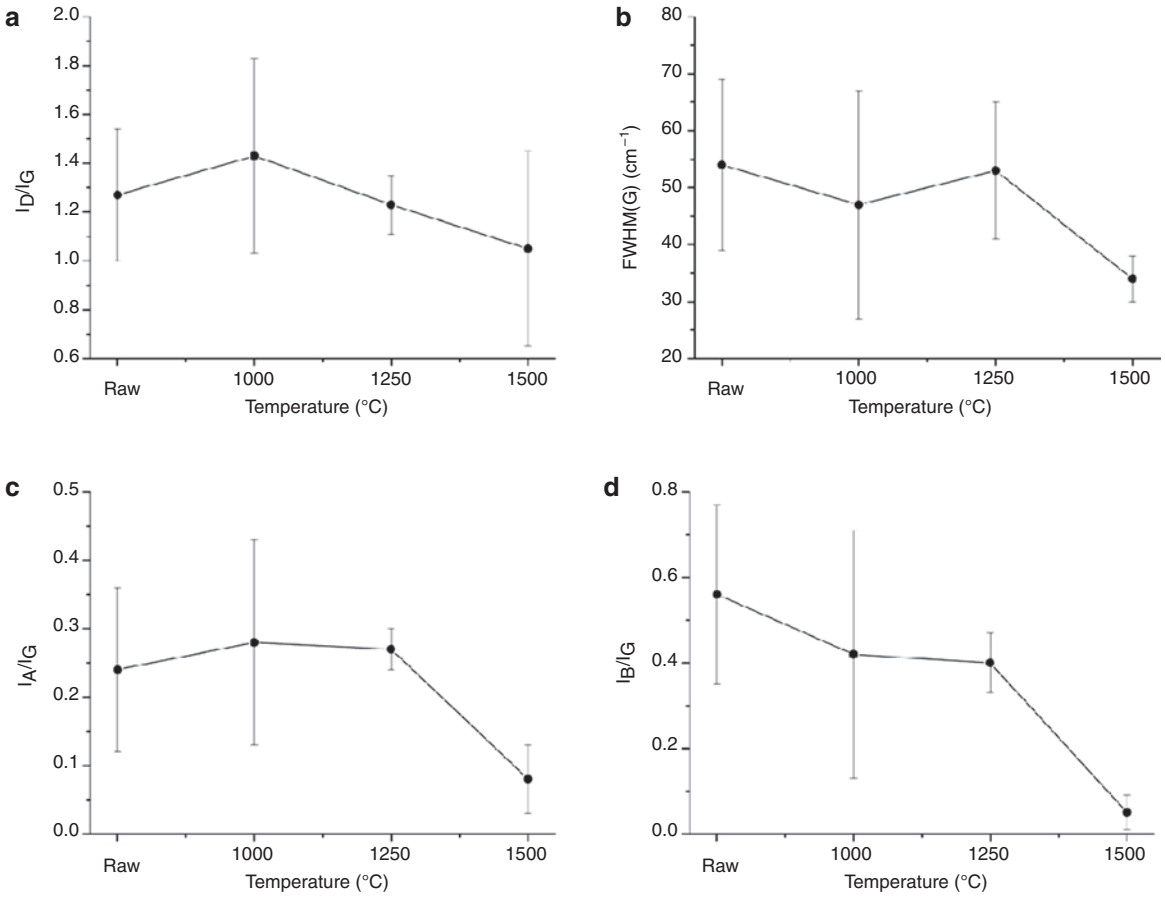

Fig. 9: (a) I_D/I_G (b) FWHM(G), (c) I_A/I_G (d) I_B/I_G parameters calculated from the deconvolution of the Raman spectra as a function of the annealing temperature.

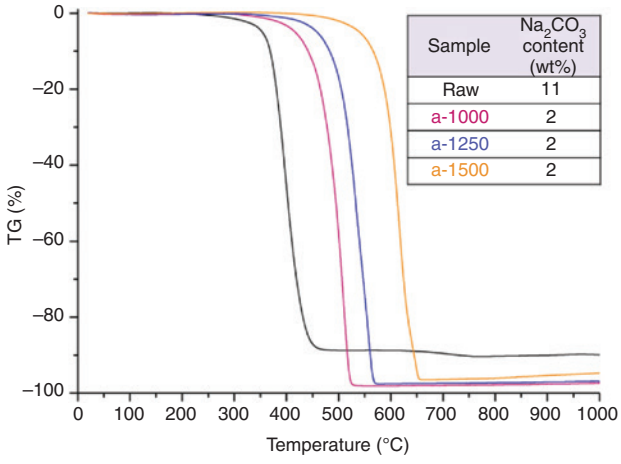

Fig. 10: TG curves (dry air, 3 °C · min^{-1}) for the samples raw, a-1000, a-1250 and a-1500.

the vapors could also be envisaged. In any case, the thermal energy of the annealing restores the graphenic foams in a first time, and improves their quality in a second time.

Thus, the use of vacuum annealing avoids the compromises relative to the variation of the parameters of the pyrolysis step, by eliminating mineral impurities and improving the crystalline quality, without any

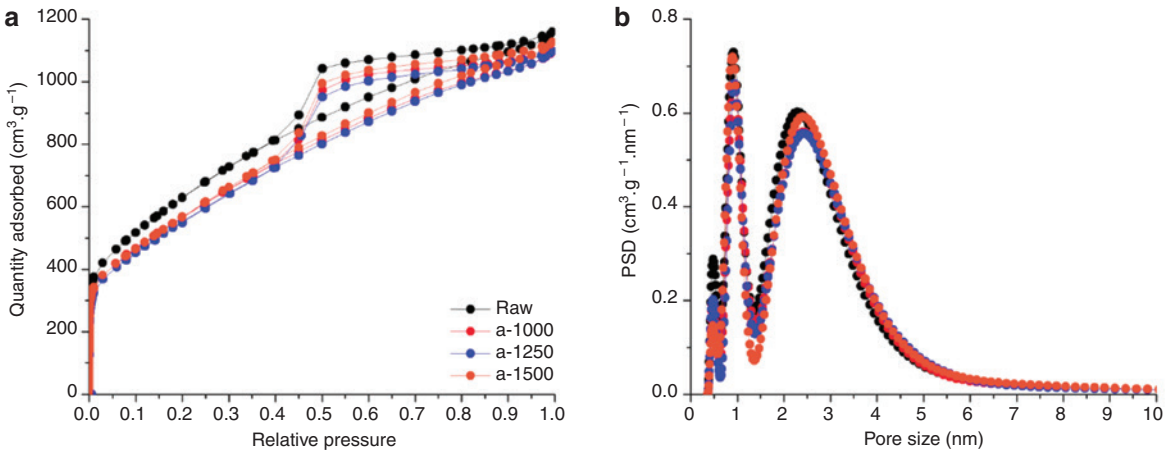

Fig. 11: (a) Adsorption isotherms (N_2 77.3 K) and (b) corresponding pore size distributions (2D-NLDFT model) for the samples raw, a-1000, a-1250 and a-1500.

Table 4: Specific surface area (BET and 2D-NLDFT models), micropore volume, total pore volume (2D-NLDFT model) for the samples raw, a-1000, a-1250 and a-1500.

Sample	BET specific surface area ($m^2 \cdot g^{-1}$)	2D-NLDFT specific surface area ($m^2 \cdot g^{-1}$)	2D-NLDFT micropore volume ($cm^3 \cdot g^{-1}$)	2D-NLDFT total pore volume ($cm^3 \cdot g^{-1}$)
Raw	2316	1840	0.59	1.67
a-1000	2068	1613	0.50	1.58
a-1250	2032	1571	0.48	1.58
a-1500	2092	1636	0.48	1.62

significant modification of the foam morphology. The higher applied temperature, 1500 °C, is the most efficient to obtain very high quality graphenic foams. Furthermore, we tried to increase the annealing time in order to obtain better improvements, and did not observe any change by modifying this parameter as most of the Na_2CO_3 is already eliminated.

Conclusion

Graphenic foams with consequent specific surface areas and high crystallinity, higher than the other results presented in the literature, were elaborated in this work via a solvothermal reaction between ethanol and sodium, and a one-step thermal treatment consisting in a pyrolysis under a nitrogen flow. The optimization of the pyrolysis step involves compromises between the structural quality of the graphenic foams and their chemical purity so, vacuum annealing has been performed in order to avoid this compromise as this post-elaboration treatment eliminates sodium carbonate while improving the crystalline quality of the foams, without damaging their structure. Then, from solvothermal sodium ethoxide, the combination of a pyrolysis under a nitrogen flow and a vacuum annealing treatment is an adapted method for the obtaining of pure high-quality graphenic foams with high accessible surface area.

Acknowledgements: The authors would like to thank Lionel Aranda for its help with the TGA measurements, Jérôme Gleize and Pascal Franchetti (LPC-A2MC laboratory, Metz, France) for their assistance during Raman spectroscopy analysis, Ghouti Medjahdi for XRD measruements, and Sylvie Migot and Jaafar Ghanbaja for TEM.

References

[1] A. C. Ferrari, F. Bonaccorso, V. Fal'ko, K. S. Novoselov, S. Roche, P. Bøggild, S. Borini, F. H. L. Koppens, V. Palermo, N. Pugno, J. A. Garrido, R. Sordan, A. Bianco, L. Ballerini, M. Prato, E. Lidorikis, J. Kivioja, C. Marinelli, T. Ryhänen, A. Morpurgo, J. N. Coleman, V. Nicolosi, L. Colombo, A. Fert, M. Garcia-Hernandez, A. Bachtold, G. F. Schneider, F. Guinea, C. Dekker, M. Barbone, Z. Sun, C. Galiotis, A. N. Grigorenko, G. Konstantatos, A. Kis, M. Katsnelson, L. Vandersypen, A. Loiseau, V. Morandi, D. Neumaier, E. Treossi, V. Pellegrini, M. Polini, A. Tredicucci, G. M. Williams, B. H. Hong, J.-H. Ahn, J. M. Kim, H. Zirath, B. J. van Wees, H. van der Zant, L. Occhipinti, A. Di Matteo, I. A. Kinloch, T. Seyller, E. Quesnel, X. Feng, K. Teo, N. Rupesinghe, P. Hakonen, S. R. T. Neil, Q. Tannock, T. Löfwander, J. Kinaret. *Nanoscale* **7**, 4598 (2014).

[2] C. Li, G. Shi. *Nanoscale* **4**, 5549 (2012).

[3] L. Jiang, Z. Fan. *Nanoscale* **6**, 1922 (2014).

[4] S. Agnoli, G. Granozzi. *Surf. Sci.* **609**, 1 (2013).

[5] C. Chang, Z. Song, J. Lin, Z. Xu. *RSC Adv.* **3**, 2720 (2013).

[6] P. Guo, H. Song, X. Chen. *Electrochem. Commun.* **11**, 1320 (2009).

[7] M. D. Stoller, S. Park, Y. Zhu, J. An, R. S. Ruoff. *Nano Lett.* **8**, 3498 (2008).

[8] X. Zhang, Z. Sui, B. Xu, S. Yue, Y. Luo, W. Zhan, B. Liu. *J. Mater. Chem.* **21**, 6494 (2011).

[9] L. Xiao, J. Damien, J. Luo, H. D. Jang, J. Huang, Z. He. *J. Power Sources* **208**, 187 (2012).

[10] S. M. Lyth, H. Shao, J. Liu, E. Akiba. *Int. J. Hydrogen Energ.* **39**, 376 (2013).

[11] J. Liu, S. Liu, T. Diao, M. S. Ismail, K. Sasaki, S. M. Lyth. *J. Electrochem. Soc.* **163**, 1049 (2016).

[12] S. M. Lyth, Y. Nabae, N. M. Islam, T. Hayakawa, S. Kuroki, M. Kakimoto, S. Miyata, *e-J. Surf. Sci. Nanotechnology* **10**, 29 (2012).

[13] K. S. Novoselov, A. K. Geim, S. V. Mozorov, D. Jiang, Y. Zhang, S. V. Dubonos, I. V. Grigorieva, A. Firsov. *Science* **306**, 666 (2004).

[14] Y. Hernandez, V. Nicolosi, M. Lotya, F. M. Blighe, Z. Sun, S. De, I. T. McGovern, B. Holland, M. Byrne, Y. K. Gun'Ko, J. J. Boland, P. Niraj, G. Duesberg, S. Krishnamurthy, R. Goodhue, J. Hutchison, V. Scardaci, A. C. Ferrari, J. N. Coleman. *Nat. Nanotechnology* **3**, 563 (2008).

[15] A. Cateline, C. Vallés, C. Drummond, L. Ortolani, V. Morandi, M. Marcaccio, M. Iurlo, F. Paolucci, A. Pénicaud. *Chem. Commun.* **47**, 5470 (2011).

[16] S. Stankovich, D. A. Dikin, R. D. Piner, K. A. Kohlhaas, A. Kleinhammes, Y. Jia, Y. Wu, S. T. Nguyen, R. S. Ruoff. *Carbon* **45**, 1558 (2007).

[17] S. Bae, H. Kim, Y. Lee, X. Xu, J. S. Park, Y. Zheng, J. Balakrishnan, T. Lei, H. R. Kim, Y. Song, Y.-J. Kim, K. S. Kim, B. Özyilmaz, J.-H. Ahn, B. H. Hong, S. Iijima. *Nat. Nanotechnology* **5**, 574 (2010).

[18] C. Berger, Z. Song, X. Li, X. Wu, N. Brown, C. Naud, D. Mayou, T. Li, J. Hass, A. N. Marchenkov, E. H. Conrad, P. N. First, W. A. de Heer. *Science* **312**, 1191 (2006).

[19] J. Cai, P. Ruffieux, R. Jaafar, M. Bieri, T. Braun, S. Blankenburg, M. Muoth, A. P. Seitsonen, M. Saleh, X. Feng, K. Müllen, R. Fasel. *Nature* **466**, 470 (2010).

[20] W. S. Hummers, R. E. Offeman. *J. Am. Chem. Soc.* **208**, 1339 (1958).

[21] M. J. McAllister, J.-L. Li, D. H. Adamson, H. C. Schniepp, A. A. Abdala, J. Liu, M. Herrera-Alonso, D. L. Milius, R. Car, R. K. Prud'homme, I. A. Aksay. *Chem. Mater.* **19**, 4396 (2007).

[22] Y. T. Chen, F. Guo, A. Jachak. *Nano Lett.* **12**, 1996 (2012).

[23] Y. Xu, K. Sheng, C. Li, G. Shi. *ACS Nano* **4**, 4324 (2010).

[24] B. G. Choi, M. Yang, W. H. Hong, J. W. Choi, Y. S. Huh. *ACS Nano* **6**, 4020 (2012).

[25] M. Choucair, P. Thodarson, J. A. Stride, *Nat. Nanotechnology* **4**, 30 (2009).

[26] H. Cui, J. Zheng, P. Yang, Y. Zu, Z. Wang, Z. Zu. *ACS Appl. Mater. Interfaces* **7**, 11230 (2015).

[27] S. L. Chou, J. Z. Wang, M. Choucair, H. K. Liu, J. A. Stride, S. X. Dou. *Electrochem. Commun.* **12**, 303 (2010).

[28] J. Z. Wang, L. Lu, M. Choucair, J. A. Stride, X. Xu, H. K. Liu. *J. Power Sources* **196**, 7030 (2011).

[29] J. Liu, D. Takeshi, K. Sasaki, S. M. Lyth. *J. Electrochem. Soc.* **161**, 838 (2014).

[30] B. Jang, E. Choi, Z. Piao. *Mater. Res. Bull.* **48**, 834 (2013).

[31] L. Speyer, S. Fontana, S. Cahen, J. Ghanbaja, G. Medjahdi, C. Hérold. *Solid State Sci.* **50**, 42 (2015).

[32] A. C. Ferrari, B. Kleinsorge, N. A. Morrison, A. Hart, V. Stolojan, J. Robertson. *J. Appl. Phys.* **85**, 7191 (1999).

[33] A. Ilie, A. C. Ferrari, T. Yagi, J. Robertson. *Appl. Phys. Lett.* **76**, 2627 (2000).

[34] A. Barreiro, F. Börnart, S. M. Avdoshenko, B. Rellinghaus, G. Cuniberti, M. H. Rümmeli, L. M. K. Vandersypen. *Sci. Rep.* **3**, 1115 (2013).

[35] S. Blazewicz, A. Swiatowski, B. J. Trznadel. *Carbon* **37**, 69 (1999).

[36] R. Andrews, D. Jacques, D. Qian, E. C. Dickey. *Carbon* **39**, 1681 (2001).

[37] E. Remy, S. Cahen, B. Malaman, J. Ghanbaja, C. Bellouard, G. Medjahdi, A. Desforges, S. Fontana, J. Gleize, B. Vigolo, C. Hérold. *Carbon* **93**, 933 (2015).

[38] S. Brunauer, P. H. Emmett, E. Teller. *J. Am. Chem. Soc.* **60**, 309 (1938).

[39] J. Rouquerol, D. Avnir, C. W. Fairbridge, D. H. Everett, J. H. Haynes, N. Pernicone, J. D. F. Ramsay, K. S. W. Sing, K. K. Unger. *Pure and Appl. Chem.* **66**, 1739 (1994).

[40] K. S. W. Sing, D. H. Everett, R. A. W. Raul, L. Moscou, R. A. Pierotti, J. Rouquerol, T. Siemieniewska. *Pure Appl. Chem.* **57**, 603 (1985).
[41] J. Jagiello, J. P. Olivier. *Carbon* **55**, 70 (2013).
[42] J. Fayos. *J. Sol. State Chem.* **148**, 278 (1999).
[43] P. D. Ownby. *J. Am. Ceram. Soc.* **75**, 1876 (1992).
[44] F. Tuinstra, J. L. Koenig. *J. Chem. Phys.* **53**, 1126 (1970).
[45] A. Eckmann, A. Felten, A. Mishchenko, L. Britnell, R. Krupke, K. S. Novoselov, C. Casiraghi. *Nano Lett.* **12**, 3925 (2012).
[46] P. Shroder, R. Nemanich, J. Glass. *Phys. Rev. B* **41**, 3738 (1990).
[47] J. Schwan, S. Ulrich, V. Batori, H. Ehrhardt. *J. Appl. Phys.* **80**, 440 (1996).
[48] A. C. Ferrari, J. Robertson. *Phys. Rev. B* **61**, 14095 (2000).
[49] L. C. Nistor, J. Van Landuyt, V. G. Ralchenko, T. V. Kononenko, E. D. Obraztsova, V. E. Strenitsky. *Appl. Phys. A* **58**, 137 (1994).
[50] Y. Hanzawa, H. Hatori, N. Yoshizawa, Y. Yamada. *Carbon* **40**, 575 (2002).